Detection of undercover karst features by geophysics (ERT) Lascaux cave hill

Cecile Verdet, Colette Sirieix, Antoine Marache, Joëlle Riss, Jean-Christophe Portais

▶ **To cite this version:**

Cecile Verdet, Colette Sirieix, Antoine Marache, Joëlle Riss, Jean-Christophe Portais. Detection of undercover karst features by geophysics (ERT) Lascaux cave hill. Geomorphology, 2020, 360, pp.1-13. 10.1016/j.geomorph.2020.107177 . hal-03166947

HAL Id: hal-03166947

https://hal.inrae.fr/hal-03166947

Submitted on 20 May 2022

HAL is a multi-disciplinary open access archive for the deposit and dissemination of scientific research documents, whether they are published or not. The documents may come from teaching and research institutions in France or abroad, or from public or private research centers.

L'archive ouverte pluridisciplinaire **HAL**, est destinée au dépôt et à la diffusion de documents scientifiques de niveau recherche, publiés ou non, émanant des établissements d'enseignement et de recherche français ou étrangers, des laboratoires publics ou privés.

Distributed under a Creative Commons Attribution - NonCommercial 4.0 International License

Version of Record: https://www.sciencedirect.com/science/article/pii/S0169555X20301495
Manuscript_a04c56a5a91da969f48ae4e75f530fbd

Detection of undercover karst features by geophysics (ERT)

- Lascaux cave hill -

Verdet Cécile[1]*, Sirieix Colette[1], Marache Antoine[1], Riss Joëlle[1], Jean-Christophe Portais[2]

* Corresponding author: cecile.verdet@u-bordeaux.fr

1 – University of Bordeaux, CNRS, Arts et Metiers Institute of Technology, Bordeaux INP, INRAE, I2M Bordeaux, F-33400 Talence, France.

2 – Ministère de la culture, Direction Régionale des Affaires Culturelles Nouvelle-Aquitaine, 54, rue Magendie, 33000 Bordeaux

Keywords: karstic morphology, ERT, Geophysics, Geostatistics model.

Abstract

The study of karst features under a detrital cover is difficult to obtain using punctual traditional tools. This paper presents a 3D geostatistical modeling of ERT (Electrical Resistivity Tomography) data to describe undercover karst features. A case study was carried out on the karstic site of the prehistoric decorated Lascaux cave (France). Geophysical measurements were used to define the limit between outcropping Coniacian or Santonian limestones (southwest) and clayey sands (northeast), with a main orientation of N140°. A geometrical description of the scarp was also constructed; pinnacles and notches were found under the clayey sand detrital formation. By combining 3D ERT with geomorphological and geological observations, the geometry of the stratigraphic limit between the Coniacian and Santonian limestone could be determined. This stratigraphic limit separates two domains, one is a potential aquifer, and acts as a feeder for the intermittent spring at the cave entrance, while the other is less permeable, resulting in a permeability contrast with the later rock type. All these observations help define the geological cave environment and ensure better protection for the paintings.

© 2020 published by Elsevier. This manuscript is made available under the CC BY NC user license
https://creativecommons.org/licenses/by-nc/4.0/

1. Introduction

In general, a karst landscape can be defined as resulting from the dissolution of carbonated rocks, such as limestone and dolomites (Mangin, 1975; Bakalowicz, 1999). The Lascaux cave is developed within the upper cretaceous limestone karst (France). It is a decorated cave that contains prehistoric paintings believed to date back to the Magdalenian era (Aujoulat *et al*., 1998). As a UNESCO world heritage site, the cave has many conservation needs: one of them is a better understanding of the surrounding area and especially of its karst. Therefore, this paper focus on the detection of undercover geomorphological karstic features localized at the northeast of the cave, *i.e.* upstream of the Lascaux cave (Xu *et al*., 2017).

The complexity of the karst is well known and its high heterogeneity can be seen as a result of a triple porosity at different scales (Király, 1975; Halihan *et al*., 1999; Worthington, 1999; Vacher and Mylroie, 2002; Ford and Williams, 2007): (1) matrix porosity, (2) fracture and crack porosity and (3) conduit porosity. The water flowing throughout these multiple porosities dissolves the rocks and finally forms characteristic geomorphological features such as sinkholes, pinnacles, karren, karst valleys, and caves. In some instances, these features are covered (or filled in the case of caves) with allochthonous or autochthonous materials such as sand and clay. Assessing these undercover karst features is quite challenging using only classical techniques like drilling, mainly because of the high variability of the karst medium. In addition, concerning the Lascaux site, only non-destructive methods can be used near the cave, so geophysical methods are suitable.

Currently, geophysical methods are widely used in large-scale investigations. To assess karst, a few techniques have proved effective: (1) ground-penetrating radar (GPR) has been used in some cases (Chalikakis *et al*., 2011; Carrière *et al*., 2013; Kaufmann and Deceuster, 2014) where the karst is not covered, especially with clay that absorbs the GPR signal; (2) microgravimetry can give good results to detect superficial empty and filled voids and to characterize karst heterogeneity (Solbakk *et al*., 2018);

(3) seismic refraction tomography is also frequently used on karst because it can give information at great depth with a high spatial resolution (Guérin *et al*., 2009; Valois *et al*., 2010, 2011); (4) finally, electrical resistivity tomography (ERT) is now widely used to characterize karstic features; to date, most of the karstic structures identified are sinkholes (Zhou *et al*., 2000; Valois *et al*., 2010; Billi *et al*., 2016; Cueto *et al*., 2018), voids (Chávez *et al*., 2018; Prins *et al*., 2019), soil and bedrock interface (Bermejo *et al*., 2016; Cheng *et al*., 2019b), and karstic aquifer geometry (Kaufmann and Deceuster, 2014; Sirieix *et al*., 2014; Carriere *et al*., 2015; Xu *et al*., 2015, 2017; Cheng *et al*., 2019a). For the Lascaux case, ERT methods have been shown to be effective (Xu *et al*., 2015).

The principle of ERT methods is to inject an electrical current between two electrodes and to measure the potential difference between two other electrodes, from which the apparent resistivity is processed. Next, an inversion process gives an image of the electrical property of the sub-surface. The image can then be interpreted as follows: resistivity depends on both the nature of the soil and on its degree of water saturation (Archie, 1942). Therefore the more saturated the soil is, the lower the resistivity, so are clay-rich soils. Most of the images are produced in 2D, thus the 3D heterogeneity of the underground is not always well sampled. For this reason, 3D ERT tools are currently considered to take account of the variability of the sub-soil.

There are three main ways to achieve 3D electrical resistivity models. First, by using what is called true 3D ERT, where both the acquisition and inversion are done in 3D. This method was applied by Chambers *et al*. (2011) to characterize a landslide, again by Chambers *et al*. (2012) to detect a bedrock under river terraces, and by Chávez *et al*. (2018) to detect a karstic void under a Mayan pyramid. True 3D ERT requires a long measuring time, and because it needs a very specific electrode geometrical arrangement in the field, it is not always achievable due to harsh terrain conditions, e.g. presence of dense vegetation. Second,the quasi-3D ERT method, where the data are acquired along 2D lines, then collated and inverted into 3D data sets. This method was used by Kneisel *et al*. (2014) to detect the depth of permafrost and its variability, with electrodes set up on a regular grid, and by Cheng *et al*.

(2019a) on karst on a large scale to detect the interface between weathered (or fractured) limestone and the unweathered bedrock. Finally, the third method is a 3D geostatistical modeling of 2D acquired and inverted ERT profile data. Geostatistical methods have been used on other resistivity data, like Riss *et al*. (2011) who used geostatistical modeling on a large set of VES (Vertical Electrical Sounding) data in order to model apparent resistivity that can be inverted as a classical 2D ERT. Other examples include: (1) the study carried out by De Benedetto *et al*. (2012) who assessed the clay content in the soil using GPR and electromagnetic induction data coupled with a geostatistical analysis;(2) Benoit *et al*. (2019) used geostatistical methods to find a correlation between hydraulic conductivity and geoelectrical data acquired with ERT and induce polarization (IP) in a riverbed. The 3D ERT geostatistical modeling method has already been applied to the south of the Lascaux cave by Xu *et al*. (2016), on a large scale. The authors revealed some interesting features, such as geological limits at a low resolution. The present study will therefore focus on a higher resolution method using 3D ERT geostatistical modeling to detect undercover karst heterogeneity and geological interfaces upstream of the Lascaux cave. The upstream area of the cave is important to acknowledge, as the water present within this area could reach the cave, depending on the spatial distribution of the heterogeneities, and their size, connectivity and permeability (Xu *et al*., 2017). Indeed, those characteristics control the water flow transporting biological or chemical compounds that could affect the painted walls. In addition, this water flow changes the internal climatic parameters, like temperature and humidity (Lacanette *et al*., 2009; Lacanette and Malaurent, 2014), challenging the cave ecosystem.

2. Study area

The study area is located in southwest France, in the Dordogne department, on the Lascaux hill, upstream of the Lascaux cave (Figure 1.a). The entrance to the cave is located about 100 m above the Vézère River. The karstic plateau that forms the hill consists of Coniacian and Santonian limestone. The northeast of the study site is covered by clayey sands (Figure 1.a) whose origin is still debated, deriving from autochthon alteration (Bruxelles and Camus, 2014; Xu *et al*., 2017) or allochthon fillings of the limestone (Lopez, 2009). Uncovered geomorphological features characterize the karst of the hill. The naturally uncovered features are sinkholes (between the study site and the Regourdou site, Figure 2), scarps (at the Regourdou site, Figure 1.b)) and a notch (Balutie archeological site and southeast of the Lascaux cave, Figure 1.c). Other known karstic features on site are few caves: Lascaux cave, small caves at the Balutie site and in the scarp southeast of the Lascaux cave. At the top of the hill, there is a site called Regourdou where the clayey sand filling was removed manually, uncovering pinnacles, caves, and scarps (Figure 1.b).

At a different scale, a map of the site shows that this study area covers middle and upper Coniacian limestone and clayey sand filling to the northeast (Figure 2). The middle and upper Coniacian (C4b, Figure 1.a) is characterized by a yellow bioclastic limestone and sandy limestone, with a presence of hummocky cross-stratification (HCS) with a thickness of 50 to 70 m. The upper part is made of a compact limestone, with an arenaceous part mixed with gravel and bioclastic debris (Guillot *et al*., 1979). The Lascaux cave developed within this upper part. At the regional scale, the very top of the Coniacian deposit is characterized by an oyster-rich level, 5 m thick (Platel, 1987), with a pale yellow limestone formations (Guillot *et al*., 1979; Platel, 1987). This level has never been described within the Lascaux cave.

The top of the hill is constituted of Santonian limestone. The lower Santonian is characterized by a chalky limestone that forms small plates, sandstone and yellow sands with a thickness between 40 and 60 m. The base level of the Santonian is formed of very small white-yellow chalky limestone with a nodulous jointing aspect (Platel, 1987). Above, a lithological ensemble is formed of a red sandy bioclastic limestone (30 to 60 m thick (Platel, 1987)). The Regourdou site is found within this part (Guillot *et al*., 1979).

The Lascaux cave seems to have developed along some of the directions that are recognized on the hill: the structural map (Figure 2) displays four main fracture families (Lopez, 2009) with directions running N178°E (F1), N119°E (F2), N93°E (F3) and N145°E (F4). These fracture directions are known at the regional scale: direction F1 is close to the Larche fault direction, direction F2 is close to that of the Condat and Cassagne faults, formed during the Hercynian orogenesis, and direction F3 is close to that of the Meyssac fault (Guillot *et al.*, 1979). The F3 and F1 families can be attributed to the tertiary tectonic and the Pyrenean orogenesis (Guillot *et al.*, 1979). Another fracture direction, F1', is proposed by Lopez (2009) that was not reported on the stereographic projection. Direction F4 is not found in the other regional faults but is a known Hercynian direction in the region (Muller and Roger, 1977). The directions of the two talwegs situated to the northwest and southeast of the cave are parallel to F4 and F1 respectively (Figure 1 and Figure 2). The main stratification plane above the Lascaux cave shows a direction of N2°E with a dip of 4 to 6°SE (Lopez, 2009, Figure 2). Regarding the geomorphological aspect, it should be noticed that the steepness of the hill slope becomes smoother at the top.

Currently, there are two main uncertainties, represented by the question marks in Figure 1d. First, the thickness of the clayey sand fillings, which is mainly unknown because of the high variability of the bedrock geometry. Second, the Santonian/Coniacian limit around the cave, the eastern clayey sand filling masks the limit at the location where the slope steepness changes. As the climatic condition of the cave depends on the water path upstream the cave, these two uncertainties will be studied and discussed further in this paper.

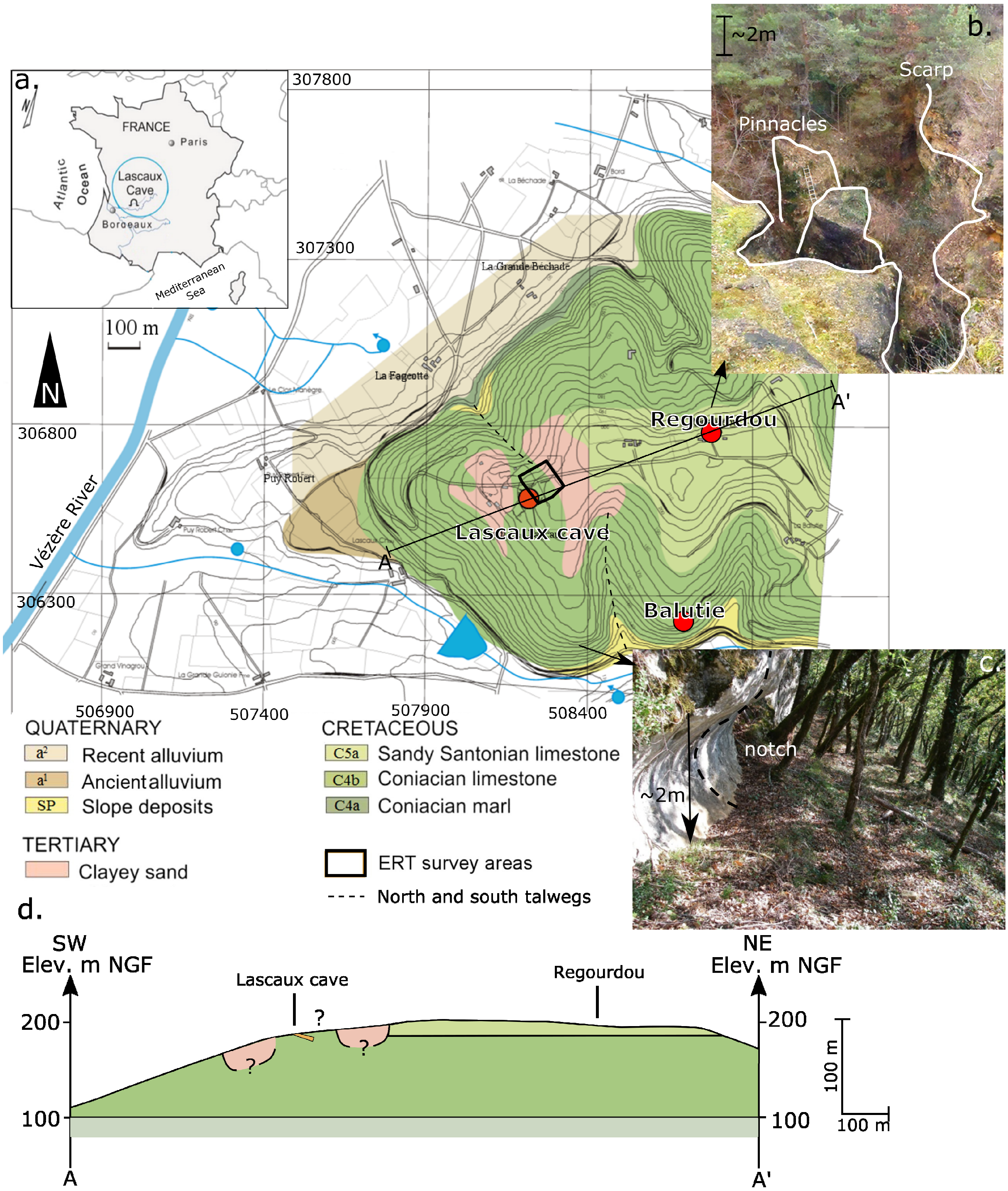

Figure 1: (a) Study area location with the geological map and site of interest (in Lopez (2009), Xu (2015) and Houillon (2016), from Schoeller (1965)), (b) Regourdou scarp and pinnacles, (c) notch, (d) section along A-A' line. Note that the vertical scale is twice the horizontal one. Question marks indicate the areas of uncertainty.

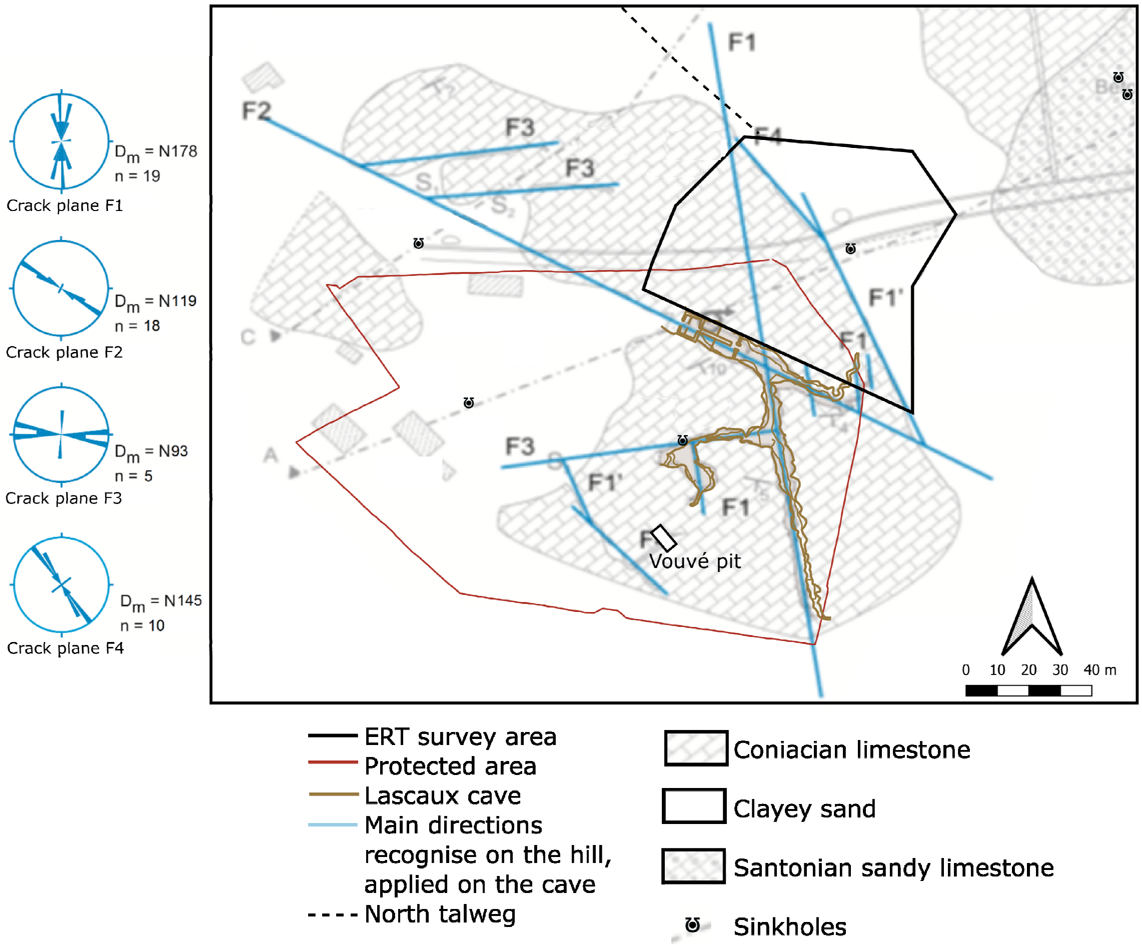

Figure 2: Known sinkhole locations superimposed on the fracture report by Lopez (2009) on a map by Vouvé (1968). "n" is the number of fractures measured on site and "Dm" is the mean direction for each fracture family.

3. Methodology

3.1. Electrical Resistivity Tomography

3.1.1. Survey design and inversion

First of all, it should be noted that on site time-lapse monitoring indicated that the best season to carry out ERT measurement on the Lascaux epikarst is from January to July, as the soil is at its highest saturation point (Xu *et al.*, 2017). A high saturation will enhance the contrast between resistive and less resistive materials, making it interesting to target such a period for the ERT measurements. We therefore chose to do the survey in March 2018.

Secondly, the surveyed area is densely forested with many anthropic features. This was the main constraint to the positioning of the ERT profiles and it conditioned the survey type. Because the true 3D process needs a precise electrode arrangement, usually a square with electrodes equally spaced on a regular mesh, the use of a true 3D technique is not easily feasible on our site. Moreover, the presence of anthropic features such as fences and buried electrical cables made 3D electrode implantation more difficult. We therefore carried out a 2D survey designed to take into account the main known directions on site, positioning the ERT lines perpendicularly to the directions. We also chose to produce a 3D geostatistical model, since Xu *et al*. (2016) demonstrated that it gave good results on this site. Xu *et al*. (2016) used a setup where the profiles were 20 m spaced among each other, with 96 electrodes spaced at 1.5 m. The spacing between profiles is large, and, as we know, the karst heterogeneity is so variable that information can be easily missed between the profiles. We reduced this spacing from 20 m in Xu *et al*. (2016) to 5-10 m between two parallel profiles. As Sirieix *et al*. (2014) showed, the smaller the electrode spacing, the better we can detect karstic features. Later, Xu *et al*. (2017) empirically demonstrated that with a 1 m electrode spacing, features could be better defined on the Lascaux hill.

In order to improve the geostatistical model accuracy, it is interesting to acquire data in at least two directions. The setup we chose is made up of 14 profiles (Figure 3). 11 profiles are made up of 72 electrodes spaced at 1 m, for a total length of 71 m (WE2-1, WE2-3, WE2-4, WE2-5; NS2-1, NS2-2, NS2-NS2-3, NS2-4, NS2-5; N100, S100); 1 profile is made up of 96 electrodes spaced at 1 m, for a total length of 95 m (WE2-2). Two profiles are refined near the cave, N50 and S50, made up of 72 electrodes spaced at 0.5 m for a total length of 35.5 m. The spacing between profiles is about 5 to 10 m, covering an area of about 5,500 m². The measurements were performed with an Iris Instrument Syscal Pro®. On each profile, the current injection is carried out during 500 ms for pole-dipole and 250 ms for gradient electrical array. The inversion is the result of a concatenation of three types of array: (1) a gradient ; (2) forward and (3) reverse pole-dipole. The gradient array was selected because of its robustness, its sensitivity to the vertical variations, its high spatial resolution and its velocity. The pole-dipole arrays were used because of their velocity, their sensibility to voids and their good penetration depth. After many tests, it appears that on the study site, the array that fitted best the depth of the compact limestone is the concatenation of those two arrays (Xu, 2015). Data were filtered in order to remove points with a quality factor above 5% (Peter-Borie *et al*., 2011). As demonstrated by Xu *et al*. (2016), the site anthropic noise is very low and can be found insignificant, the size of the electrode spacing is adapted and a very small number of datum points were filtered. As a result, most of the profiles kept their total number of datum points. On the worst-case scenario (profile WE2-4), only 9 datum points out of 9,133 were removed. The inversion was performed with Res2DInv® software (Loke, 2004) v. 4.05.38. with L1 norm as it is adapted on a heterogeneous medium with abrupt variability, which is the case for the karst. The mesh was refined to half the electrode spacing. The absolute error of the models was between 0.34% and 3.9%. After inversion, the total number of resistivity datum points was 32,845.

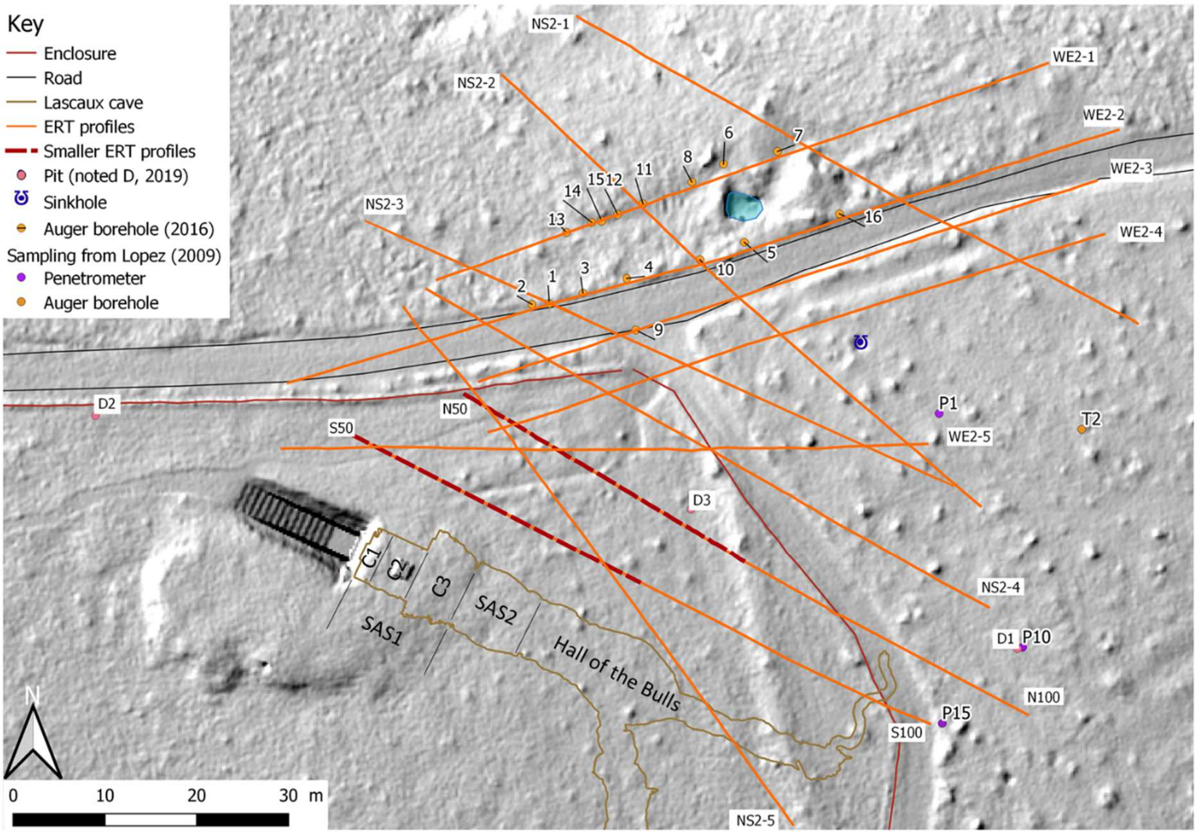

Figure 3: ERT profiles, augers (numbered 1-16), penetrometers (labeled P1, P10, P15), and small pits (labeled D1-D3) location on a DEM (Digital Elevation Model) by Muth (2017). SAS1 is the first airlock, composed of three compartments C1, C2 and C3 and SAS2 is the second airlock. No paintings are present in the two airlocks.

The experimental one-off sampling plan comprised cone penetrometer test (CPT) data acquired by Lopez (2009) near the area of investigation (Figure 3). It was completed by superficial auger boreholes along the WE2-1 and WE2-2 profiles. These data (Figure 4) are to be used later in the paper to complete the interpretation of the 3D geostatistical model, alongside the other geomorphological observations made on the hill (see “study area” description). Also, two small pits were dug in July 2019, marked D1 and D3 in Figure 3, and gave a direct view of the first 40 centimeters. Pit D1 was dug in the clayey sand area, D3 in the limestone area (Figure 1.a).

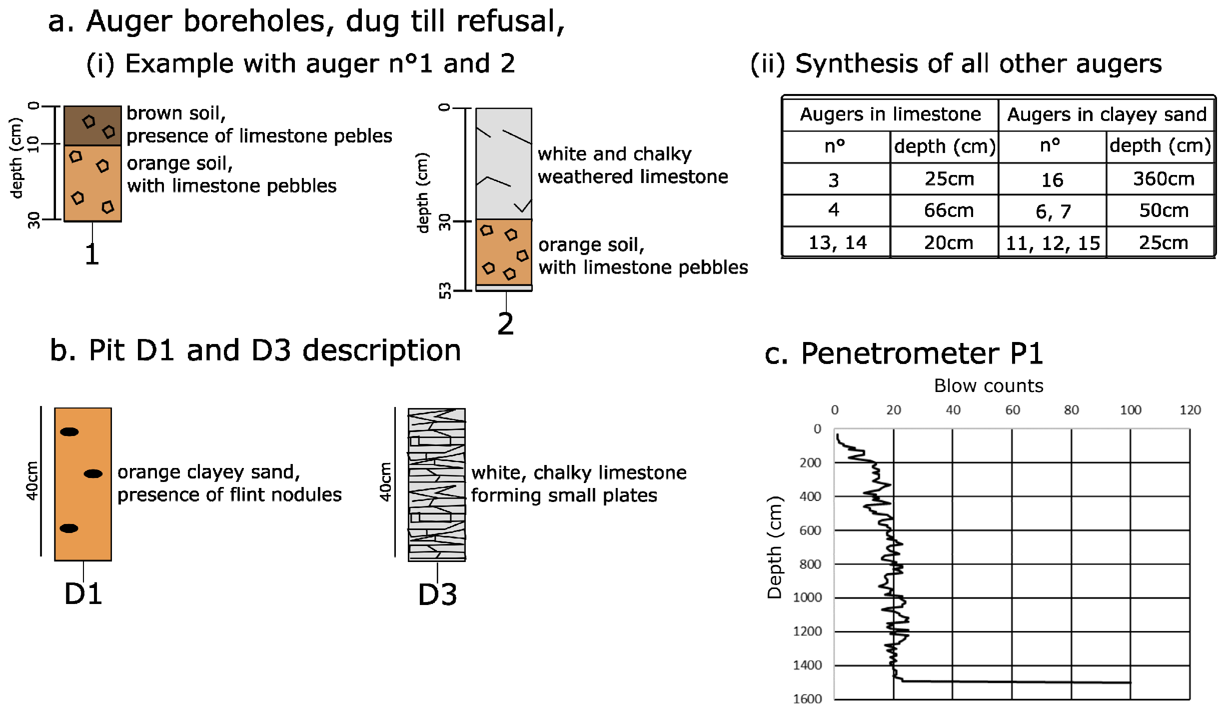

Augers in limestone		Augers in clayey sand	
n°	depth (cm)	n°	depth (cm)
3	25cm	16	360cm
4	66cm	6, 7	50cm
13, 14	20cm	11, 12, 15	25cm

Figure 4: description of (a) auger boreholes with (a.i) augers n°1 and 2 in example, and (a.ii) synthesis of the refusal depth for augers showing limestone materials and depth investigated (not to the refusal) for augers showing clayey sand formation with flint nodules; (b) description of pits D1 and D3; (c) penetrometer P1 result, with a refusal depth at 15m.

3.1.2. 2D results

Each 2D electrical resistivity image displayed the same pattern of resistivity (Figure 5):

- In the northeast area of the profile (to the right of limits B and C), there is a part with a globally low resistivity, and with a high inner variability. Field observations, augers and pit D1 (Figure 4.b) showed that this part is mainly formed of clayey sand. At the surface, some highly resistive patches are present, which are the signature of clearer sand.
- In the southwest, at depth (below limits A and C) there is a globally high resistivity part with a low variability. As Verdet *et al*. (2018) and Xu *et al*. (2016, 2015) showed, such resistivity is due to the massive limestone bedrock. This is also supported by penetrometer P1 (Figure 4.c) data that gave a refusal depth of 15 m (Figure 3).

- In the southwest, near the surface (to the left of limit B, above limit A), there is a mildly resistive part with an inner variability. Xu *et al*. (2017) indicated that this part is made up of different limestones from the previous one. They also indicated that this limestone has a resistivity that varies with time; therefore, its water content evolves. This superficial part was called weathered Coniacian limestone by Houillon (2016) and Xu *et al*. (2016), corresponding to the epikarst as defined by Mangin (1975).

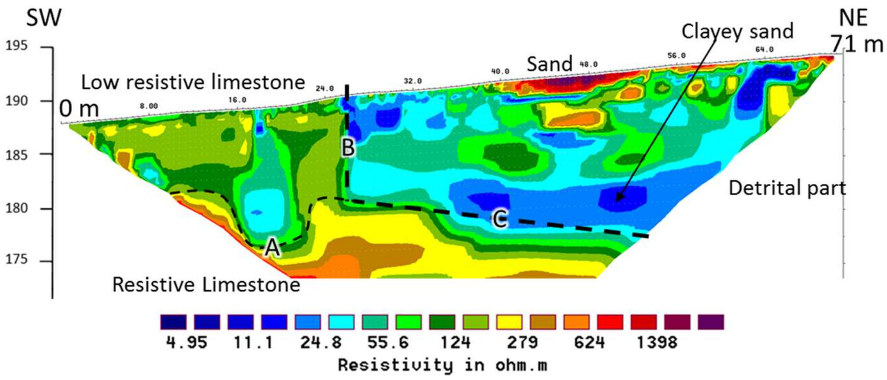

Figure 5: WE2-4 profile with the geological interpretation reported.

3.2. 3D geostatistical modelling

Several steps make up the geostatistical modeling process. The first is to statistically observe the raw inverted data. The mean resistivity is 164 Ω·m, varying from 3 to 5,119 Ω·m. In order to perform the variographic calculus, giving an understanding of the spatial structure of our data, and to avoid any influence from extreme values, we kept values between 10 and 1,000 Ω·m (representing 98% of all values, *i.e.* 32,250 values). As these extreme values could have a physical significance, they are added for the final 3D kriging modeling process. The variogram study and the kriging model are made from the $\log_{10}$ of the resistivity and are transformed into resistivity at the end for the final analysis.

The first tool we use is a variographic map (variomap), enabling us to observe the data structure in all directions. In particular, it makes anisotropy stand out (if anisotropy exists for the studied variable), and gives correlation length(s). The first map is computed using the ERT data from the whole study area. On this map, two anisotropic directions are unveiled: one in the horizontal plane, with direction N140°, and one vertically (Figure 6.a and c). We can see that the variomap (Figure 6.a) remains isotropic under 10 m in the horizontal plane.

A second variomap is built using ERT data from the limestone part only, in the southwest of the study area. The N140° direction present on the whole site does not appear, nor does any other anisotropy direction in the horizontal plane (Figure 6.b). Only a vertical anisotropy appears (Figure 6.d), as the one found over the whole study area.

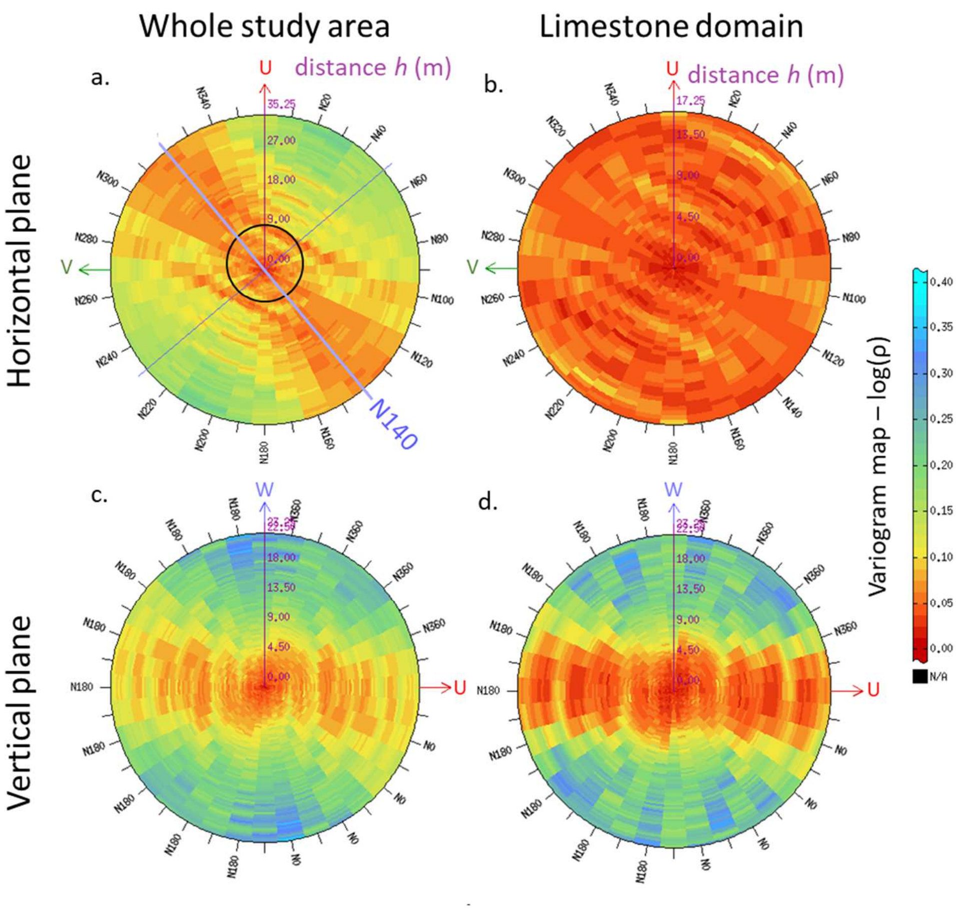

Figure 6: Variographic maps for (a and c) the whole study area, and (b and d) the limestone area only. (a and b) represents the horizontal plane and (c and d) represents the vertical plane. $\vec{U}$, $\vec{V}$ and $\vec{W}$ are the three vectors giving the three main orientations of the 3D space. The color scale represents the log(ρ) variogram value.

The experimental variogram is then calculated in two directions: one in the horizontal plane and one in the vertical plane. The experimental variogram in the horizontal plane is calculated isotopically as the neighborhood will have a radius of 10 m for the kriging process (see below). The corresponding theoretical variogram is then fitted on the experimental variogram as a combination of four elementary models (Figure 7), providing that the lag stays under 10 m so the N140° anisotropy direction can be ignored:

- A nugget effect with a sill at 0.015;
- A spherical model with a sill at 0.035, a range of 7 m in the horizontal plane and 1.5 m in the vertical plane;
- A second spherical model with a sill at 0.018, a range of 6 m in the horizontal plane and 500 m in the vertical plane;
- A cubic model with a sill of 0.19, a range of 500 m in the horizontal plane and 25 m in the vertical plane.

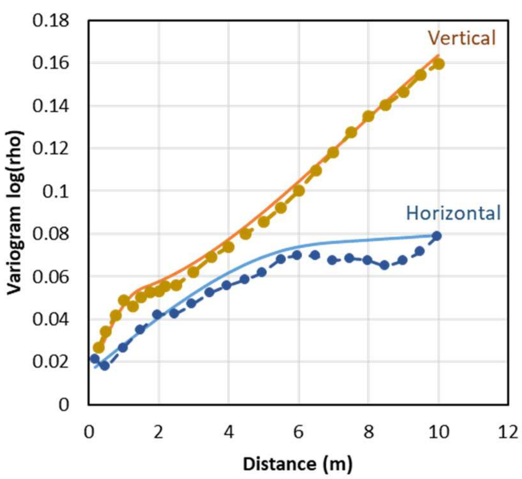

Figure 7: Experimental (dotted lines) and theoretical (continuous lines) variograms in both horizontal and vertical planes.

In order to validate the variogram model, a cross-validation can be performed. The cross-validation is a process that compares the true measured values to the values estimated by kriging at the same points. The validation coefficient calculated with this method is 0.95, based on 32,250 experimental data. Given this coefficient and this very large number of points, we consider that the variogram model is validated.

After this variographical study, the next goal is to estimate a resistivity value at each node of a regular grid by the kriging method. The chosen grid has an elemental cell size of 0.5m x 0.5m x 0.5m, because of the size of the inversion grid used with the geophysical software. The kriging needs a defined neighborhood to determine the volume around a grid node for which the resistivity value will be estimated. The experimental points within this neighborhood will be used for the estimation at the grid node. In our case, this neighborhood is a 10 m diameter sphere. The total number of estimated points after kriging is 1,246,592.

Then the model is intercepted with the Digital Elevation Model (DEM, X. Muth, personal communication) in order to remove estimated points above the topographical surface.

4. Results and discussion

The 3D electrical model obtained is shown in Figure 8. Already, a few features stand out, such as the N140° orientation. The geological limits are outlined later in this section ; so are the geomorphologic karstic features under the cover of other detrital material.

4.1. Geological limit precision

First of all, the 3D resistivity model can be divided into two main domains, separated by the N140° vertical limit already found with the variogram maps. The two domains can be interpreted with the help of auger boreholes, penetrometer data, small pits (Figure 3 and Figure 4) and old pictures of the cave entrance, before being widened (Figure 9). The N140° direction could correspond to the N145° structural direction cited earlier. Looking at the structural map (Figure 2), the N145° (F4) direction seems to separate the limestone part from the detrital part. Xu *et al*. (2016) also found a structural direction of N145° by geostatistics, to the south and next to our study site, on the Lascaux hill.

Secondly, in the northeast, the first domain has a mainly low resistivity with a median of 68 Ω·m (Figure 8). In the southeast of the domain, a very superficial zone appears with a maximum thickness of 2 m and a very high median resistivity of 640 Ω·m. The low resistivity part is made up of detrital clayey-sand, found with augers 6, 7, 8, 11, 12, 15 and 16 (Figure 3). The high resistivity part is composed of sands that can be observed at the surface, directly on the floor and in pit D1 (Figure 3). These formations were also characterized in the southern part of the site by Xu *et al*. (2016) and Bruxelles and Camus (2014), Xu (2015).

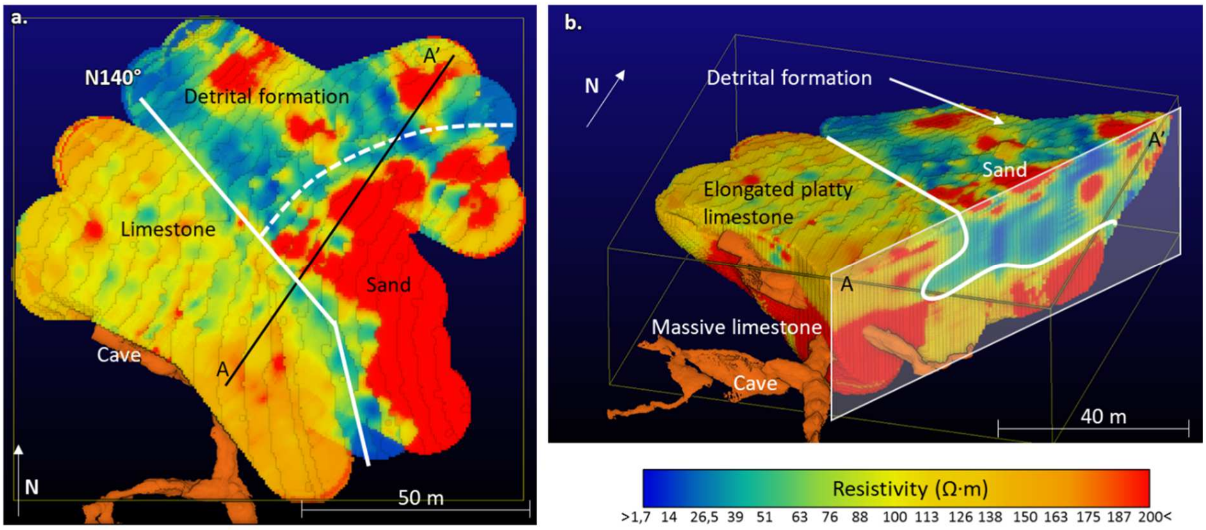

Figure 8: 3D resistivity model interpreted using auger and Vouvé boreholes. (a) View from above, with the superficial limits and the A-A' section position. (b.) View from the south, with a section along A-A' that shows the internal structure.

In the southwest, the second domain has a globally higher resistivity, attributed to limestone, as it has been found in augers 1, 2, 3, 4, 5, 10, 13 and 14 (Figure 3). It can be separated into two subzones (Figure 8.b.):

- a superficial one, above 181 mNGF (French ordnance datum), heterogeneous with a median resistivity of 140 Ω·m. The entrance of the cave develops within this subzone;

- a deeper one, below 181 mNGF, and more homogeneous, with a higher median resistivity of 493 Ω·m. The Hall of the Bulls (Figure 3), one of the decorated chambers of Lascaux, as well as the rest of the cave develops within this resistive subzone.

Xu *et al.* (2016) also identified these two domains at a wider scale and south of our study site, with a median resistivity of 150 and 556 Ω·m respectively, and an elevation of the limit of 179 mNGF. These values are virtually the same, allowing for measurement accuracy. Auger reconnaissance (n°1, 2, 3, 4, 13, 14, Figure 4.a) and Vouvé boreholes (sampled from 1965 to 1968, described and published *in* Xu (2015)) show that the whole zone is made up of limestone. The top part (above 181 mNGF) has a low, variable resistivity, probably indicating a limestone with a globally high porosity and water or clay content; while the lower part has a higher resistivity, thus more homogeneous, indicating a more massive limestone. The limit between these two kinds of limestone found with the geophysical ERT method is therefore between 181 mNGF ± 1.5 m (this study) and 179 mNGF ± 2 m (Xu *et al*., 2016). The uncertainty about the altitude is determined from the size of the inversion blocks at this depth.

We observe an outcrop on historical pictures of the site (Figure 9). At the top of Figure 9.a (above approx. 185 mNGF) and in Figure 9.b, we can see a limestone made up of elongated small plates with a filling in between the joints. Between 185 and 183 mNGF (Figure 9.a), the limestone is covered with calcite, but seems to consist of the same elongated small plates. Such a limestone, which is easily weathered, could perfectly explain the low resistivity of 140 Ω·m found previously for the top part. The top limestone can also be observed in the recent pit D3 (190 mNGF) as centimetric chalky, slightly red and yellow, with elongated small plates, and a clayey-sand filling in the joints. In the south, an old pit (Vouvé pit in Figure 2), dug in the 1960's and partially filled since, allows direct observation of the limit between the two limestones (Figure 10). This clearly delineated boundary is estimated at around 182 mNGF in the Vouvé pit, in good agreement with a sedimentary origin well known in the literature (Platel, 1987) rather than an erosion origin.

Figure 9: Historic picture of the cave entrance before it was widened. (a) SAS1 C3 is now located here (see Figure 3). The limits of approx. 185.5 and 183 mNGF are estimated from the recent 3D model of the cave (picture Windels 1940-1941). (b) It is known that the feet of Laval are above 183mNGF, so the whole outcrop is above 183mNGF. The SAS1-C1 is now located here (picture Larivière 1940-09, Brive, from right to left: M. Breuil, Marsal (discoverer), Ravidat (discoverer) and Laval)). We can observe in the upper part that the limestone forms elongated small plates with a filling in between the joints.

Figure 10: Limit between elongated small plates and compact limestone observed in the Vouvé pit south of the cave (downstream). (Picture Verdet).

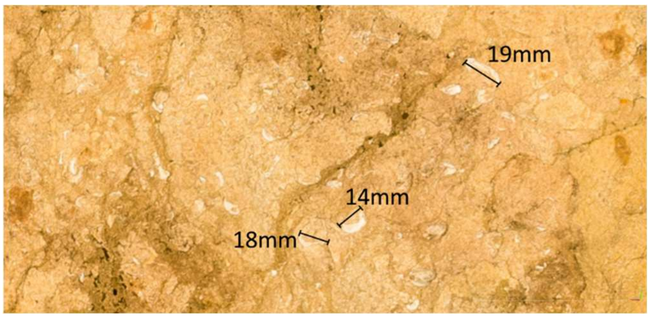

Figure 11: Detail of the oyster-rich level seen in the roof of the "Hall of the Bulls" (Picture Studio Guichard/Pérazio Engineering).

The deeper part with a higher resistivity (493 Ω·m) is made up of a more compact limestone, as can be observed within the cave and on the historical photo in Figure 9.a, Figure 10 and Figure 11, below the approximate 183 mNGF limit. It is mostly covered with calcite, and where visible, it forms multi-decimetric slabs. We also observed an oyster-rich level in the roof of the “Hall of the Bulls”, at an altitude of 181-182 mNGF (Figure 11), making it a part of the massive limestone. The oysters observed measure about 1 to 2cm, so they could be *Ceratostreon pliciferum auricularis.* We have also found this oyster-rich level in other parts of the cave, always between 178 mNGF and 182 mNGF. The geological log for the Perigordian Region (Guillot *et al*., 1979; Platel, 1987) shows that such an oyster-rich level is the last stratigraphic level of the upper Coniacian stage, with no oysters found in the lower Santonian limestone. So, the oyster-rich level observed in the cave defined the limit between Coniacian limestone and the Santonian limestone on the site.

Besides the limit altitude of 182 mNGF defined by the oyster-rich level, the altitude is quite constant across the whole site in the ERT model (this study, Xu *et al*. (2016)), with a very small dip, if any. The N140° direction – or any other horizontal anisotropy direction – has not been found on the variographic map computed on the limestone part (Figure 6.c), showing that the two kinds of limestone, each with its own lithology, must be homogeneous – horizontally and at our scale – with a sub-horizontal dip.

Previously, other authors (Lopez, 2009; Houillon, 2016; Verdet *et al*., 2016; Xu *et al*., 2016, 2017) said that the difference between the two parts (top with a resistivity of 140 Ω·m, and bottom with a resistivity of 493 Ω·m) was due only to the difference in weathering effect. On the top was a limestone identified as the epikarst, and below a limestone identified as the infiltration/transmission zone (Houillon, 2016). In this present study, the dip of the limit between the two limestones is sub-horizontal (close to the one found by Lopez (2009)) and the thickness of the top layer is not constant (thicker at the top than at the bottom of the site, and the top layer of limestone was never found to the west of the studied site). These observations are not consistent with the hypothesis of a difference in weathering according to depth as the only explanation for this top layer.

Moreover, the nature of the two kinds of limestone is not the same. Platel (Guillot *et al.,* 1979 and Platel, 1987 completed with a personal communication, 2019) described the lower Santonian limestone as isotropic and chalky, forming centimetric chips separated by marly beds. Platel (1987, and personal communication, 2019) described the top of the upper Coniacian as a shelly limestone, rich in oysters 2 to 3 cm in size, marking a visible limit with the Santonian limestone. Furthermore, on the Guillot *et al.,* (1979) geological map, the geological limit clearly follows the topography around the hill, forming a smoother plateau at the top. The limit is roughly at an altitude between 180 and 190 mNGF. What we observe throughout this study is consistent with the Platel description. Therefore, we conclude that the top part, with a low resistivity, is made up of Santonian limestone, whereas the bottom part, with a higher resistivity, is made up of Coniacian limestone. Moreover, the Santonian limestone constitution makes it prone to a higher alteration than the Coniacian, and it is highly weathered on site. The elevation of the limit between these two kinds of limestone is determined from the 3D model (this study, the Xu *et al*. (2016) study) and the field observations between 179 and 183 mNGF on the study site. The synthesis of all our observations allows us to estimate the altitude of this limit at around 182 mNGF. From this point, the Coniacian/ Santonian limit on the geological map is modified, as shown in Figure 13. This changes the Vouvé idea (chapter “Vouvé" *in* Leroi-Gourhan and Allain (1979)) that described the permeable limit as a marly horizon as the origin of the waterflow in the SAS1 C3. Originally, Schoeller (1965) described this horizon as a small layer, 30-40 cm thick, made up of a high water content limestone. Recently, Houillon *et al.* (2017) described a contrast in permeability –rather than a marly horizon– allowing the water to flow into the cave at the roof of SAS1 C3 (Figure 3). Our study confirms the Schoeller (1965) description; besides, we think the contrast in permeability is due to the contact between the compact Coniacian limestone limit and the Santonian limestone with the weathered Santonian limestone acting as a potential aquifer for the water flowing at the intermittent spring at the cave entrance.

4.2. Karst geomorphological aspect

The analysis of the whole resistivity model showed there are two main resistivity groups. They are delimited by an arbitrary limit, based on the resistivity histogram: one above 250 Ω·m and the other below 250 Ω·m. The materials left when keeping the resistivity of the blocks (from the 3D model) below 250 Ω·m comprise mainly the detrital clayey-sand formations and the platy limestone (Santonian limestone). We chose here to focus on the shape of the compact limestone that emerged when we keep the blocks with resistivity higher than 250 Ω·m. The depth of the compact limestone under the detrital formation is confirmed by penetrometer P1 (Figure 3) by Lopez (2009) showing a refusal depth at the same depth, *i.e.* at 176 mNGF. Most of the decorated part of the cave is located under this limit, and therefore develops within the massive Coniacian limestone.

The vertical limit between the limestone and the detrital domains becomes clear and stands as a scarp with a few notch zones (Figure 12), as observed at the Regourdou site (Figure 1.b.), to the south of the hill site (Figure 1.c.), and at the Balutie site. This is also supported by earlier on site work by Vouvé (Chapter Vouvé *in* Leroi-Gourhan and Allain (1979)) that showed the limit between the two domains must form a scarp. We can also observe that the Coniacian limestone roof forms what could be interpreted as karren morphologies between the scarp and the cave, with the karren channels highlighted with dotted lines.

At the bottom of the detrital domain, the limestone shape becomes clearer as well and defines what can be assimilated as pinnacles (Figure 12). This interpretation is coherent with the observations made at the Regourdou site (Figure 1.b.) where pinnacles are visible.

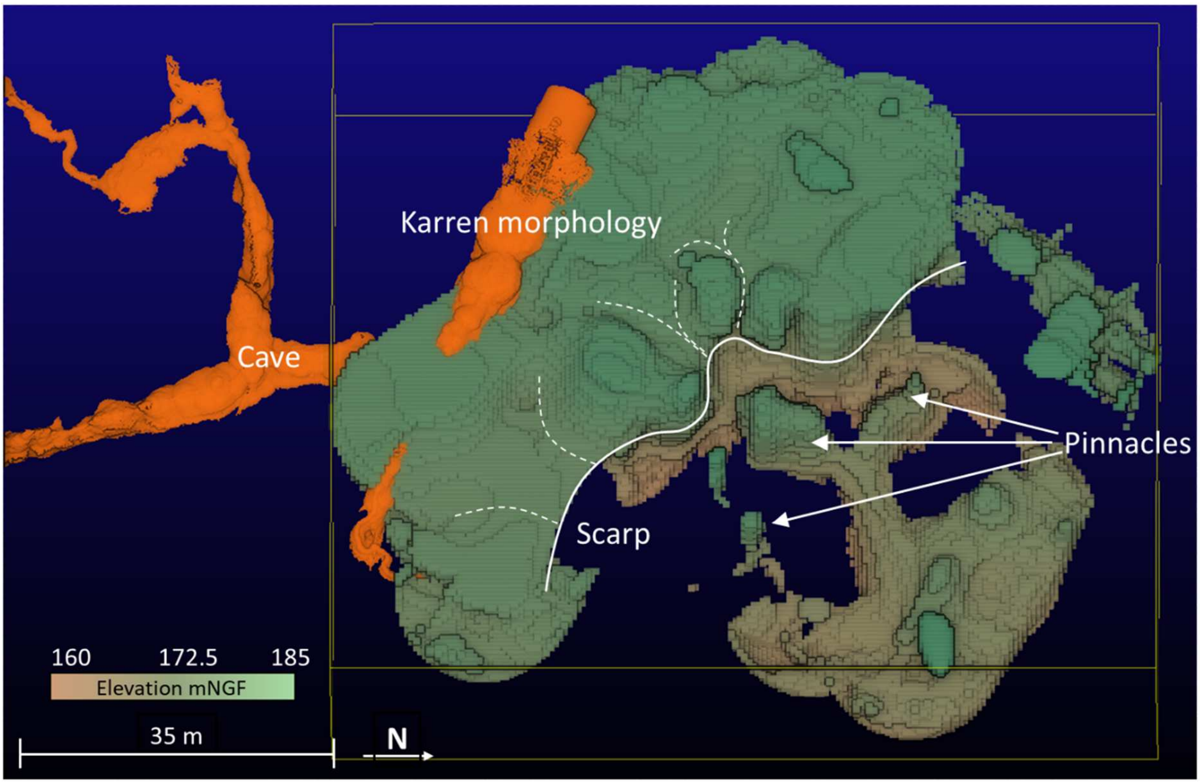

Figure 12: View of the compact limestone. The plain arrows point to the pinnacles, the scarp is well defined. Karren morphology can also be observed (dotted lines) at the top of the limestone, north of the cave.

The area upstream of the Lascaux cave shows a precise organization of its karstic features as described earlier in this paper, such as under-cover pinnacles, a notch and the limestone depth and geometry.

The geometry of the superficial limit of the limestone and clayey sand formation (Figure 8.a) can be reported at the scale of the hill (Figure 13.a). We observe that the northwest part of the limit has the same N140° orientation as the NW talweg (N137°) and prolongs it (Figure 13). We can assume that N140° is a fracture direction, which allowed the NW talweg to form (Figure 13). We can also assume that this fracture allowed the formation of a depression. Vouvé (chapter Vouvé *in* Leroi-Gourhan and Allain, 1979) showed there are two paleo-tributaries of the Vézère paleo-river present on the Lascaux hill, one at each side of the cave. We can assume that the south bank of the northern tributary could be the scarp that we found delimiting the limestone and the detrital clayey sand formation. The geological section is modified, as shown in Figure 13.b.

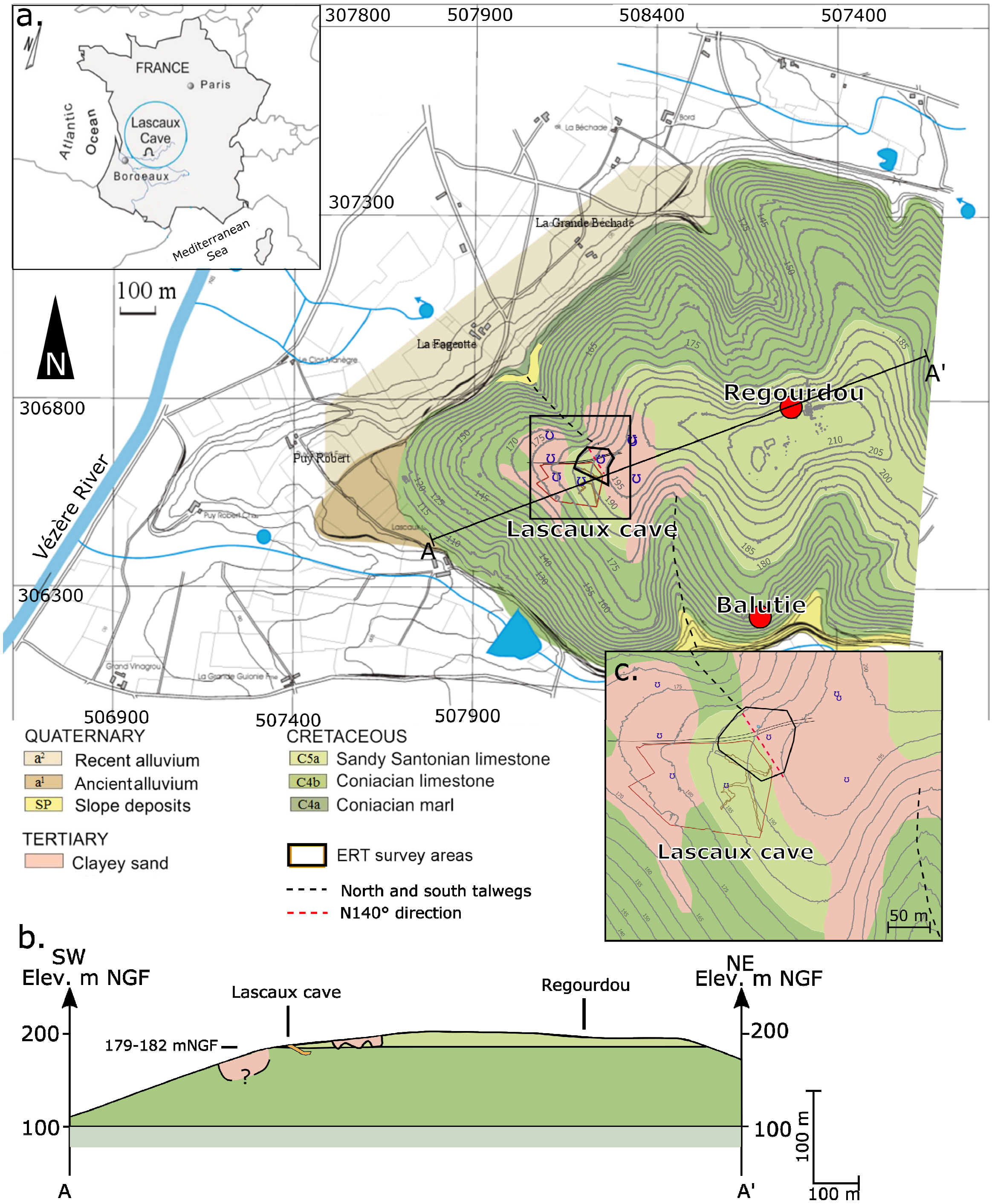

Figure 13: (a) Modified geological map according to the findings of this present study. (b) Section along A-A' line. Note that the Santonian limit and the depth of the NE sand filling are determined. The nature of the pinnacle is unknown, but could be made up of Santonian. (c) Close-up of the study zone.

5. Conclusion

The construction of a geostatistical 3D model based on ERT data provided a better understanding of the Lascaux cave karstic environment geometry. The study area upstream of the cave shows two areas, with a NW-SE limit separating limestones in the west from a clayey sand formation in the east. This limit is an extension of the north talweg and is a structural direction. The high resolution of the 3D ERT model uncovered unknown features of the site, such as pinnacles and a limit between the two kinds of limestone. The limit between the upper Coniacian limestone and the lower Santonian limestone has been redrawn thanks to geological and geomorphological observations on site along with the 3D ERT model in order to match the 182 mNGF isohypse. We now assume that the entrance to the cave develops within the small elongated chalky Santonian limestone plates; while the rest of the cave, which is decorated, develops within the massive Coniacian limestone. Due to its constitution, the Santonian limestone is more prone to weathering than the Coniacian, and therefore has a higher permeability. It is likely a potential aquifer acting as a feeder for the intermittent spring at the cave entrance. The water flowing through this intermittent spring can transport biological or chemical compounds that could affect the painted walls, inducing potential conservation matters. In the northeast of the site, the clayey sand formation lies above a limestone that forms undercover pinnacles and a scarp.

Geological knowledge of the area around the cave is of great interest for its conservation. The limit between the limestone and the detrital clayey sand formation to the northeast of the cave is well known and could be used for protection purposes. The changes we have made to the Coniacian and Santonian limit (more fractured, with clayey sand joint fillings and a higher water content) can be used to adapt models of the cave environment, e.g. the thermal properties of the rocks around the cave or the hydrogeological models applied to water circulation around the cave. Finally, the contrast in permeability allows the presence of a perched aquifer, which feeds the spring at the entrance of the cave. The permeability contrast is not due to a marly horizon; but to the contact between the lower platty and permeable Santonian limestone and the upper compact shelly Coniacian limestone with a lower permeability. It explains why the emergence in the cave entrance is located at this altitude and at the limit between the Santonian and Coniacian limestones.

Acknowledgements

The authors would like to thank the French Ministry of Culture (DRAC Nouvelle-Aquitaine) for accessing the cave surroundings and for their financial support. We especially thank Philippe Malaurent for his help on the site and on the history of the site. He forms part of the memory of the Lascaux cave. We also thank Fabien Naessens and Sylvain Mateo for their help with the field surveys (ERT and sampling). We are very grateful to Jean-Pierre Platel for sharing his geological knowledge of the region and Laurent Londeix for his help on the geology.

References

Archie, G.E., 1942. The electrical resistivity log as an aid in determining some reservoir characteristics, in: Transaction of American Institute of Mining, Metallurgical, and Petroleum Engineers. Dallas, pp. 54–62.

Aujoulat, N., Cleyet-Merle, J.-J., Gaussen, J., Tisnerat, N., Valladas, H., 1998. Approche chronologique de quelques sites ornés paléolithiques du Périgord par datation Carbone 14 en spectrométrie de masse par accélérateur de leur mobilier archéologique. Paléo 319–323.

Bakalowicz, M., 1999. Connaissance et gestion des ressources en eaux souterraines dans les regions karstiques. (Guide technique No. 3). Agence de l'eau Rhône-Méditérrannée-Corse, Lyon.

Benoit, S., Ghysels, G., Gommers, K., Hermans, T., Nguyen, F., Huysmans, M., 2019. Characterization of spatially variable riverbed hydraulic conductivity using electrical resistivity tomography and induced polarization. Hydrogeol. J. 27, 395–407. https://doi.org/10.1007/s10040-018-1862-7

Bermejo, L., Ortega, A.I., Guérin, R., Benito-Calvo, A., Pérez-González, A., Parés, J.M., Aracil, E., Bermúdez de Castro, J.M., Carbonell, E., 2016. 2D and 3D ERT imaging for identifying karst morphologies in the archaeological sites of Gran Dolina and Galería Complex (Sierra de Atapuerca, Burgos, Spain). Quat. Int. 433, 393–401. https://doi.org/10.1016/j.quaint.2015.12.031

Billi, A., De Filippis, L., Poncia, P.P., Sella, P., Faccenna, C., 2016. Hidden sinkholes and karst cavities in the travertine plateau of a highly-populated geothermal seismic territory (Tivoli, central Italy). Geomorphology 255, 63–80. https://doi.org/10.1016/j.geomorph.2015.12.011

Bruxelles, L., Camus, H., 2014. Grotte de Lascaux. Formes et formations anciennes de surface et sub-surface. (rapport d'étude No. PRO-R-2014-03). Inrap, Protée et Ceneau, Montignac, Dordogne.

Carriere, S.D., Chalikakis, K., Danquigny, C., Clement, R., Emblanch, C., 2015. Feasibility and limits of electrical resistivity tomography to monitor water infiltration through karst medium during a rainy event, in: Hydrogeological and Environmental Investigations in Karst Systems. Springer, pp. 45–55.

Carrière, S.D., Chalikakis, K., Sénéchal, G., Danquigny, C., Emblanch, C., 2013. Combining Electrical Resistivity Tomography and Ground Penetrating Radar to study geological structuring of karst Unsaturated Zone. J. Appl. Geophys. 94, 31–41. https://doi.org/10.1016/j.jappgeo.2013.03.014

Chalikakis, K., Plagnes, V., Guerin, R., Valois, R., Bosch, F.P., 2011. Contribution of geophysical methods to karst-system exploration: an overview. Hydrogeol. J. 19, 1169–1180. https://doi.org/10.1007/s10040-011-0746-x

Chambers, J.E., Wilkinson, P.B., Kuras, O., Ford, J.R., Gunn, D.A., Meldrum, P.I., Pennington, C.V.L., Weller, A.L., Hobbs, P.R.N., Ogilvy, R.D., 2011. Three-dimensional geophysical anatomy of an active landslide in Lias Group mudrocks, Cleveland Basin, UK. Geomorphology 125, 472–484.

Chambers, J.E., Wilkinson, P.B., Wardrop, D., Hameed, A., Hill, I., Jeffrey, C., Loke, M.H., Meldrum, P.I., Kuras, O., Cave, M., Gunn, D.A., 2012. Bedrock detection beneath river terrace deposits using three-dimensional electrical resistivity tomography. Geomorphology 177–178, 17–25. https://doi.org/10.1016/j.geomorph.2012.03.034

Chávez, R.E., Tejero-Andrade, A., Cifuentes, G., Argote-Espino, D.L., Hernández-Quintero, E., 2018. Karst Detection Beneath the Pyramid of El Castillo, Chichen Itza, Mexico, by Non-Invasive ERT-3D Methods. Sci. Rep. 8, 15391. https://doi.org/10.1038/s41598-018-33888-9

Cheng, Q., Chen, X., Tao, M., Binley, A., 2019a. Characterization of karst structures using quasi-3D electrical resistivity tomography. Environ. Earth Sci. 78, 285. https://doi.org/10.1007/s12665-019-8284-2

Cheng, Q., Tao, M., Chen, X., Binley, A., 2019b. Evaluation of electrical resistivity tomography (ERT) for mapping the soil–rock interface in karstic environments. Environ. Earth Sci. 15.

Cueto, M., Olona, J., Fernández-Viejo, G., Pando, L., López-Fernández, C., 2018. Karst-induced sinkhole detection using an integrated geophysical survey: a case study along the Riyadh Metro Line 3 (Saudi Arabia). Surf. Geophys. 12.

De Benedetto, D., Castrignano, A., Sollitto, D., Modugno, F., Buttafuoco, G., Papa, G. lo, 2012. Integrating geophysical and geostatistical techniques to map the spatial variation of clay. Geoderma 171–172, 53–63. https://doi.org/10.1016/j.geoderma.2011.05.005

Ford, D., Williams, P.W., 2007. Karst hydrogeology and geomorphology, Rev. ed. ed. John Wiley & Sons, Chichester, England ; a Hoboken, NJ.

Guérin, R., Baltassat, J.-M., Boucher, M., Chalikakis, K., Galibert, P.-Y., Girard, J.-F., Plagnes, V., Valois, R., 2009. Geophysical characterisation of karstic networks – Application to the Ouysse system (Poumeyssen, France). Comptes Rendus Geosci. 341, 810–817. https://doi.org/10.1016/j.crte.2009.08.005

Guillot, P.-L., Feys, R., Lefavrais-Raymond, A., Platel, J.-P., Lefavrais-Henry, M., 1979. Notice de la carte géologique de ka France à 1/50 000 - Terrasson (n°784).

Halihan, T., Sharp Jr, J.M., Mace, R.E., 1999. Interpreting flow using permeability at multiple scales. Karst Model. Karst Waters Inst. Spec. Publ. 5, 82–96.

Houillon, N., 2016. La dynamique du carbone inorganique dans le continuum sol-épikarst-cavité du site de la Grotte de Lascaux (Dordogne, France): apports des monitorings hydrogéochimique et microclimatique continus pour l'étude de l'aérologie et le développement d'une méthode de simulation des processus calco-carboniques aux parois (Thèse). Université de Bordeaux.

Houillon, N., Lastennet, R., Denis, A., Malaurent, P., Minvielle, S., Peyraube, N., 2017. Assessing cave internal aerology in understanding carbon dioxide (CO2) dynamics: implications on calcite mass variation on the wall of Lascaux Cave (France). Environ. Earth Sci. 76. https://doi.org/10.1007/s12665-017-6498-8

Kaufmann, O., Deceuster, J., 2014. Detection and mapping of ghost-rock features in the Tournaisis area through geophysical methods—an overview. Geol. Belg. 17, 17–26.

Király, L., 1975. Rapport sur l’état actuel des connaissances dans le domaine des caractères physiques des roches karstiques. Hydrogeol. Karstic Terrains Hydrogéologie Terrains Karstiques Int. Union Geol. Sci. 53–67.

Kneisel, C., Emmert, A., Kästl, J., 2014. Application of 3D electrical resistivity imaging for mapping frozen ground conditions exemplified by three case studies. Geomorphology 210, 71–82. https://doi.org/10.1016/j.geomorph.2013.12.022

Lacanette, D., Malaurent, P., 2014. Prévision climatique 3D dans la grotte de Lascaux. Karstologia 49–57.

Lacanette, D., Vincent, S., Sarthou, A., Malaurent, P., Caltagirone, J.-P., 2009. An Eulerian/Lagrangian method for the numerical simulation of incompressible convection flows interacting with complex obstacles: Application to the natural convection in the Lascaux cave. Int. J. Heat Mass Transf. 52, 2528–2542. https://doi.org/10.1016/j.ijheatmasstransfer.2008.12.028

Leroi-Gourhan, A., Allain, J., 1979. Lascaux inconnu. CNRS.

Loke, M.H., 2004. Tutorial : 2-D and 3-D electrical imaging surveys.

Lopez, B., 2009. Les processus de transfert d’eau et de dioxyde de carbone dans l’épikarst (Thèse). University of Bordeaux.

Mangin, A., 1975. Apport de l’hydrodynamique pour la compréhension des aquifères karstiques (Thèse). Université de Dijon.

Muller, J., Roger, P., 1977. L’Evolution structurale des Pyrénées (Domaine central et occidental). Le segment hercynien, la chaîne de fond alpine. Géologie Alp. 149–191.

Muth, X., 2017. DEM of the Lascaux hill.

Peter-Borie, M., Sirieix, C., Naudet, V., Riss, J., 2011. Electrical resistivity monitoring with buried electrodes and cables: noise estimation with repeatability tests. Surf. Geophys. 9, 369–380. https://doi.org/10.3997/1873-0604.2011013

Platel, J.-P., 1987. Le crétacé supérieur de la plate-forme septentrionale de Bassin d’Aquitaine. stratigraphie et évolution géodynamique. (Thèse). Université Bordeaux III.

Prins, C., Thuro, K., Krautblatter, M., Schulz, R., 2019. Testing the effectiveness of an inverse Wenner-Schlumberger array for geoelectrical karst void reconnaissance, on the Swabian Alb high plain, new line Wendlingen–Ulm, southwestern Germany. Eng. Geol. 249, 71–76. https://doi.org/10.1016/j.enggeo.2018.12.014

Riss, J., Luis Fernández-Martínez, J., Sirieix, C., Harmouzi, O., Marache, A., Essahlaoui, A., 2011. A methodology for converting traditional vertical electrical soundings into 2D resistivity models: Application to the Saïss basin, Morocco. GEOPHYSICS 76, B225–B236. https://doi.org/10.1190/geo2010-0080.1

Schoeller, H., 1965. Étude géologique, hydrogéologique et climatologique de la grotte de Lascaux pendant le cycle 1964-1965. Rapp. Détude 30.

Sirieix, C., Riss, J., Rey, F., Prétou, F., Lastennet, R., 2014. Electrical resistivity tomography to characterize a karstic Vauclusian spring: Fontaine d’Orbe (Pyrénées, France). Hydrogeol. J. 22, 911–924. https://doi.org/10.1007/s10040-013-1095-8

Solbakk, T., Fichler, C., Wheeler, W., Lauritzen, S.-E., Ringrose, P., 2018. Detecting multiscale karst features including hidden caves using microgravimetry in a Caledonian nappe setting: Mefjell massif, Norway. Nor. J. Geol. https://doi.org/10.17850/njg98-3-04

Vacher, H.L., Mylroie, J.E., 2002. Eogenetic karst from the perspective of an equivalent porous medium. Carbonates Evaporites 17, 182.

Valois, R., Bermejo, L., Guérin, R., Hinguant, S., Pigeaud, R., Rodet, J., 2010. Karstic morphologies identified with geophysics around Saulges caves (Mayenne, France). Archaeol. Prospect. 17, 151–160. https://doi.org/10.1002/arp.385

Valois, R., Camerlynck, C., Dhemaied, A., Guerin, R., Hovhannissian, G., Plagnes, V., Rejiba, F., Robain, H., 2011. Assessment of doline geometry using geophysics on the Quercy plateau karst (South

France): morphology of dolines using geophysics. Earth Surf. Process. Landf. 36, 1183–1192. https://doi.org/10.1002/esp.2144
Verdet, C., Sirieix, C., Riss, J., 2018. Détermination du fonctionnement hydrogéologique d'un site karstique par un suivi temporel en tomographie de résistivité électrique – Epikarst de la grotte de Lascaux, in: Actes Du 11ème Colloque de Géophysique Des Sols et Des Formations Superficielles. Presented at the 11e Colloque GEOFCAN, Anthony, pp. 81–84.
Verdet, C., Xu, S., Sirieix, C., Riss, J., Allègre, V., 2016. Cluster analysis of time-lapse resistivity data to identify a privileged feed zone within the epikarst of Lascaux Cave (France). Presented at the 43rd IAH International Congress: "Groundwater and society: 60 years of IAH," Montpellier, p. 127.
Vouvé, J., 1968. Travaux préliminaires dans le cadre de l'aménagement d'un nouvel accès dans la grotte de Lascaux - Creusement d'un puits. Ministère des Affaires Culturelles, Périgueux.
Worthington, S.R., 1999. A comprehensive strategy for understanding flow in carbonate aquifers. Karst Model. Eds Palmer MV Palmer ID Sasowsky Spec. Publ. 30–37.
Xu, S., 2015. Caractérisation de l'environnement karstique de la grotte de Lascaux par couplage de méthodes géophysique, statistique et géostatistique (Thèse). Université de Bordeaux.
Xu, S., Sirieix, C., Ferrier, C., Lacanette-Puyo, D., Riss, J., Malaurent, P., 2015. A geophysical tool for the conservation of a decorated cave – a case study for the Lascaux cave. Archaeol. Prospect. 22, 283–292. https://doi.org/10.1002/arp.1513
Xu, S., Sirieix, C., Marache, A., Riss, J., Malaurent, P., 2016. 3D geostatistical modeling of Lascaux hill from ERT data. Eng. Geol. 213, 169–178. https://doi.org/10.1016/j.enggeo.2016.09.009
Xu, S., Sirieix, C., Riss, J., Malaurent, P., 2017. A clustering approach applied to Time-Lapse ERT interpretation - case study of Lascaux Cave. J. Appl. Geophys. https://doi.org/10.1016/j.jappgeo.2017.07.006
Zhou, W., Beck, B.F., Stephenson, J.B., 2000. Reliability of dipole-dipole electrical resistivity tomography for defining depth to bedrock in covered karst terranes. Environ. Geol. 39, 760–766.